

Raman-Polarization-Fluorescence Spectroscopic Lidar for Real-Time Detection of Humic-like Substance Profiles

Zhongwei Huang, Yongkai Wang, Tian Zhou, Yuanzong Ji, Jianrong Bi, Jinsen Shi, Hui Wen, and Jianping Huang*



Cite This: *Environ. Sci. Technol.* 2025, 59, 7235–7245



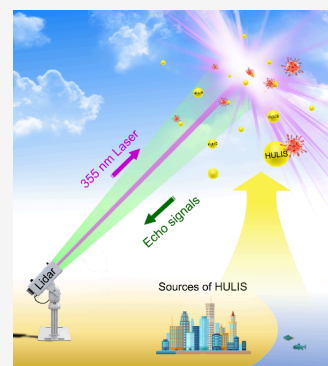
Read Online

ACCESS |

Metrics & More

Article Recommendations

ABSTRACT: Humic-like substances (HULIS) widely exist in the atmosphere and may strongly affect human health, environment, and climate. However, there are still no accurate methods for detecting the vertical distribution of HULIS. Here, a Raman-Polarization-Fluorescence Spectroscopic Lidar (RPFSL) was developed to simultaneously measure 64-channel broad fluorescence spectra (370–710 nm) of atmospheric aerosols at an excitation wavelength of 355 nm. The study revealed that dust could be coated by abundant fluorescent substances, with a maximum fluorescence efficiency reaching 0.15. Moreover, the fluorescent spectra of air pollutants exhibited a unimodal structure, while the spectra of dust exhibited three peaks, suggesting that they may be useful for highly accurate identification of dust aerosols from other aerosols. The findings in this study were confirmed by near-ground air sampling analysis based on fluorescence excitation–emission matrix-parallel factor (EEM-PARAFAC) methods; we demonstrated that HULIS and protein-like organic matter (PLOM) were the main components of fluorescent aerosols during the study period. During air pollution events, the number concentration of HULIS reached up to 9699 particles·m⁻³. For the first time, this study proposes a real-time, high-resolution method for detecting height-resolved HULIS, significantly helping to evaluate the environmental and health implications of HULIS.



KEYWORDS: Lidar, Humic-like substances, Fluorescent aerosols, Dust, Polarization

1. INTRODUCTION

HULIS, a class of high-molecular-weight organic substances, are ubiquitous within the realms of clouds, fog, rainwater, and atmospheric aerosol particles.^{1,2} HULIS are rich in polycyclic aromatic hydrocarbons, phenolic compounds, and acidic functional groups. The name originates from the analogy of their ultraviolet and fluorescence properties to those of humic acid derived from aquatic and terrestrial sources.³ HULIS are a vital component of water-soluble organic carbon (WSOC) and secondary organic aerosols (SOA) in the atmosphere, consisting of 9 to 72% of WSOC.⁴ HULIS are generated from a variety of sources, including biomass combustion,⁵ vehicular exhaust gases,⁶ marine emissions,⁷ and secondary atmospheric reactions.⁸ They significantly influence atmospheric processes, e.g., the formation of cloud condensation nuclei (CCN),⁹ serve as vectors and oxidants for organic pollutants in the atmosphere,¹⁰ enhance the reflectivity of individual particles due to their hygroscopic nature,¹¹ and engage in the absorption of ultraviolet light, thereby triggering a cascade of radiative transfer and photochemical reactions.¹²

At present, HULIS monitoring is mainly carried out near the ground, including HULIS separation extraction and quantitative analysis.^{13–17} Laser-induced fluorescence (LIF) technology is a popular method for real-time monitoring and identification of HULIS.¹⁸ Under the excitation of different

ultraviolet laser wavelengths, various types of fluorescent substances exhibit unique absorption and emission spectra, with peak fluorescence wavelengths showing significant differences under specific excitation wavelengths. Chen et al. recently used a combination of solvent extraction and solid-phase extraction to separate HULIS from the sampled total suspended particulates, and determine their optical characteristics based on ultraviolet–visible absorption spectra and excitation–emission matrices (EEM).¹⁹ Alternatively, HULIS in fluorescent aerosol particles can be distinguished using online measurements from LIF-based instrument (such as wideband integrated bioaerosol sensor, WIBS).²⁰ However, current measurements of HULIS are only conducted near the surface of the ground due to the limitation of detecting methods.^{21,22}

It is known that there are plenty of HULIS in higher altitude because of often dynamic and thermodynamic processes in the atmosphere. However, until now there have been no reports on

Received: January 2, 2025

Revised: March 2, 2025

Accepted: March 4, 2025

Published: March 12, 2025



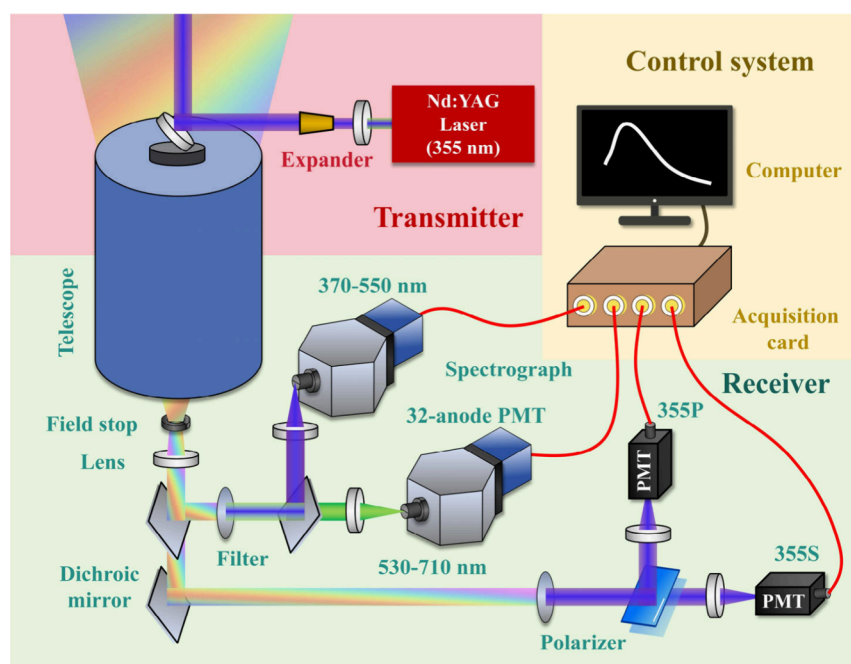


Figure 1. Schematics of the Raman-Polarization-Fluorescence Spectroscopic Lidar (RPFSL) developed by Lanzhou University and used in this study.

observations of HULIS at such heights. Long-term continuous measurements of vertical distribution of HULIS could be obtained by remote sensing technology. Fluorescence lidar can monitor the origins, transport pathways, and spatiotemporal dynamics of fluorescence aerosols.^{23–25} However, in the real atmosphere, the fluorescence aerosols excited by ultraviolet light are mostly complex mixtures, and the measured fluorescence spectra result from the superposition of spectra from different fluorophores. This complexity brings a big challenge for quantifying atmospheric fluorescent aerosols. Existing fluorescence lidar typically records only the total or parts of fluorescence of aerosols, leading to lack of sufficient information for identifying and quantifying individual classes of fluorescent particles or assessing their contribution to the total signal.^{26–28}

To fill the gap, we developed a Raman-Polarization-Fluorescence Spectroscopic Lidar (RPFSL), capable of observing the 64-channel fluorescent spectrum of atmospheric aerosols between 370 and 710 nm, with an excitation wavelength of 355 nm. The system was deployed during an intensive observation period (IOP) of dust-bioaerosol (DuBi) in Northern China, from April to May 2016. The vertical structure of fluorescent aerosols was profiled under different weather conditions, and a novel method for quantifying the HULIS concentration profiles in the atmosphere was proposed.

2. MATERIALS AND METHODS

2.1. Raman-Polarization-Fluorescence Spectroscopic Lidar (RPFSL). The RPFSL, developed by Lanzhou University, used a Nd:YAG laser operating at a frequency of 20 Hz, delivering a pulse energy of 80 mJ at 355 nm. Backscattering signals were collected via a telescope with a diameter of 350 mm. Subsequently, the received signal at 355 nm was divided by a polarization beam splitter (PBS) into parallel and perpendicular components. The full-band fluorescent spectrum of atmospheric aerosols excited at 355

nm was detected by two Licel 32-channel spectrometers, with a spectral resolution of 5.8 nm. Limited by the signal-to-noise ratio (SNR) of the fluorescence signal, the maximum height is set to 600 m. The lidar system is designed with a coaxial structure to control the signal blind zone within 100 m, maximizing the detection of signals from the ground to higher altitude. The combination of the two spectrometers is carried out using an overlapping method for signal acquisition. The signal intensity of each spectral channel normalized against the intensity of the Raman scattering channel for N₂ (387 nm), to effectively mitigate the influence of the geometric form factor of the lidar system. Finally, an overlap factor matrix for each channel obtained by experimental way is used to perform crosstalk correction of the grating spectrometer. The spatial and temporal resolutions for Mie signals were 3 min and 3.75 m, respectively, while those for fluorescence signals were 3 min and 15 m. Fluorescence measurements were conducted exclusively during the night to avoid solar background radiation. Thus, the RPFSL was capable of recording the full fluorescence spectra (370–710 nm, 64 channels) of atmospheric aerosols under varying weather conditions. Figure 1 schematically illustrates the RPFSL used in this study.

2.2. Retrieval Methods. Raw signals were preprocessed through background subtraction, range correction, overlap correction, and polarization calibration.^{29,30} The backscattering coefficient at 355 nm and the fluorescence backscattering coefficient were calculated using the Raman method.³¹

The general lidar equation for Mie channels is as follows:

$$P_M = O(z) \frac{1}{z^2} C_M (\beta_M^a + \beta_M^m) \exp \left\{ -2 \int_0^z (\alpha_M^a + \alpha_M^m) dz' \right\} \quad (1)$$

where P_M is the backscattered signal intensity, $O(z)$ is the geometrical overlap factor, and C_M is the lidar system constant. Backscattering and extinction coefficients contain the contributions of aerosols and molecules, $\beta_M^a + \beta_M^m$ and $\alpha_M^a + \alpha_M^m$ respectively.

For Raman channels, the backscattered signal intensity (P_R) can be rewritten as

$$P_R = O(z) \frac{1}{z^2} C_R \beta_R \exp \left\{ - \int_0^z (\alpha_M^a + \alpha_R^a + \alpha_M^m + \alpha_R^m) dz' \right\} \quad (2)$$

Here, β_R and α_R are the backscattering and extinction coefficients at a certain Raman wavelength, λ_R .

In the case of fluorescence, the backscattering signal intensity within the spectral interval (λ_{\min} , λ_{\max}) can be derived using eq 3:³²

$$P_F = O(z) \frac{1}{z^2} \exp \left\{ - \int_0^z (\alpha_M^a + \alpha_M^m) dz' \right\} \cdot \int_{\lambda_{\min}}^{\lambda_{\max}} \int_{r_{\min}}^{r_{\max}} C_F(\lambda) \times N_F \times \delta_F \times \exp \left\{ - \int_0^z (\alpha_F^a(\lambda, z') + \alpha_F^m(\lambda, z')) dz' \right\} dr d\lambda \quad (3)$$

Here, δ_F ($d\delta_F(\lambda, r)/d\lambda$) is the cross-section of spectral differential fluorescence, and N_F ($dN(r)/dr$) is the concentration of fluorescent aerosol particles.

The Mie backscattering coefficient, β_M , can be obtained from the ratio of eq 1 and (2):

$$\beta_M = \frac{C_R P_M}{C_M P_R} \beta_R \frac{\exp \left\{ - \int_0^z (\alpha_R^a + \alpha_R^m) dz' \right\}}{\exp \left\{ - \int_0^z (\alpha_M^a + \alpha_M^m) dz' \right\}} \quad (4)$$

Similar to Mie scattering, by introducing the fluorescence backscattering coefficient, β_F , β_F can be obtained from the ratio of eq 2 and (3):

$$\beta_F = \int_{\lambda_{\min}}^{\lambda_{\max}} \int_{r_{\min}}^{r_{\max}} N_F \times \delta_F dr d\lambda = \frac{C_R P_F}{C_F P_R} \beta_R \frac{\exp \left\{ - \int_0^z (\alpha_R^a + \alpha_R^m) dz' \right\}}{\exp \left\{ - \int_0^z (\alpha_F^a(\lambda, z') + \alpha_F^m(\lambda, z')) dz' \right\}} \quad (5)$$

The depolarization ratio is an important factor for characterizing the nonsphericity degree of atmospheric aerosols, widely used for identification of spherical and nonspherical particles, particularly in dust detection.^{33–35} The particle depolarization ratio (PDR), δ_p , is given by eq 6:^{36,37}

$$\delta_p = \frac{(1 + \delta_m)\delta_v R - (1 + \delta_v)\delta_m}{(1 + \delta_m)R - (1 + \delta_v)} \quad (6)$$

where δ_m is the molecular depolarization ratio (the typical value is 0.00376), δ_v is the volume depolarization ratio, and R is the total backscattering to air molecule backscattering ratio.³⁸

The fluorescence intensity is correlated with the aerosol density and fluorescence efficiency. The fluorescence efficiency (η) is calculated following the method proposed by Sugimoto et al.,³⁹ i.e., the fluorescence efficiency is considered an effective indicator of aerosol fluorescence, suggesting that higher fluorescence efficiency corresponds to more intense aerosol fluorescence.

$$\eta = f \frac{SSA}{1 - SSA} \cdot \frac{\beta_F}{\beta_M} \quad (7)$$

Here, f is the difference between the Mie scattering phase function and that for fluorescence, SSA is the aerosol single-scattering albedo. In this study, we assumed that the SSA of aerosols during a floating dust event and a clear day is 0.9 but 0.95 (0.99) for a heavy dust event (air pollution event).⁴⁰

The vertical distribution of HULIS concentration (N_H) could be calculated using the formula as shown in eq 8.

$$N_H = K_H \cdot \frac{\beta_H}{\delta_F} \quad (8)$$

Here, K_H denotes the proportion of HULIS in atmospheric fluorescent aerosols. Since there is currently no reported data on the proportion of high-altitude fluorescent aerosols, and HULIS is a class of water-soluble organic mixtures with high relative molecular weight,⁴¹ in this study, we use the proportion of HULIS analyzed in the ground-based aerosol samples in Figure 7c to estimate the proportion of HULIS within the total fluorescent aerosol. β_H is the fluorescence backscattering coefficient of HULIS. The results of Figure 7d show that the peak fluorescence of HULIS mainly appeared at 420–500 nm, exhibiting a distinct single-peak structure, while other bands show weaker fluorescence. Consequently, we hypothesize that the fluorescence backscattering coefficient at the peak wavelength of HULIS can be completely regarded as the fluorescence backscattering coefficient of HULIS. The spectral range is given and β_H can be calculated by substituting eq 5. The fluorescence scattering cross-section at 355 nm, was estimated at 10^{-12} cm² sr⁻¹ nm⁻¹, adopting a reference value from previously published studies.^{42,43}

2.3. EEM-PARAFAC Analysis. Parallel factor analysis (PARAFAC) is an efficient tool for decomposing fluorescence excitation–emission matrices (EEMs) into intrinsic chemical components. In this study, drEEM toolbox, developed by Murphy et al.,⁴⁴ was employed for the PARAFAC analysis of raw EEMs. Initially, the EEM data were normalized using the total fluorescence intensity of each sample. Subsequently, the EEM spectra were scrutinized individually to exclude samples with anomalous signals. The stability and reliability of the model were ascertained by integrating the randomness of residuals, core consistency, split-half analysis, and visualizing spectral loadings. The optimal number of fluorescent components was determined, ultimately leading to the identification of excitation and emission spectra and the maximum fluorescence intensity for each component.

3. MAIN RESULTS

Lidar measurements from the RPFSL were conducted from April to May 2016 in Zhangbei (114.7°E, 41.2°N; altitude: 1393 m a.s.l), China. The lidar site was predominantly influenced by dust storms and pollution originating from anthropogenic combustion in the spring, rendering it an ideal location for examining the mixing of dust and anthropogenic pollution in Asia. During the observation period, PM_{2.5}, PM₁₀, and absorption coefficients were concurrently monitored at the lidar site. PM_{2.5} and PM₁₀ were collected using Tapered Element Oscillating Microbalance Monitors (TEOM RP1400), and the absorption coefficient was derived from the black carbon concentration measured using an aethalometer (AE31). During the study time, we selected five representatives of three

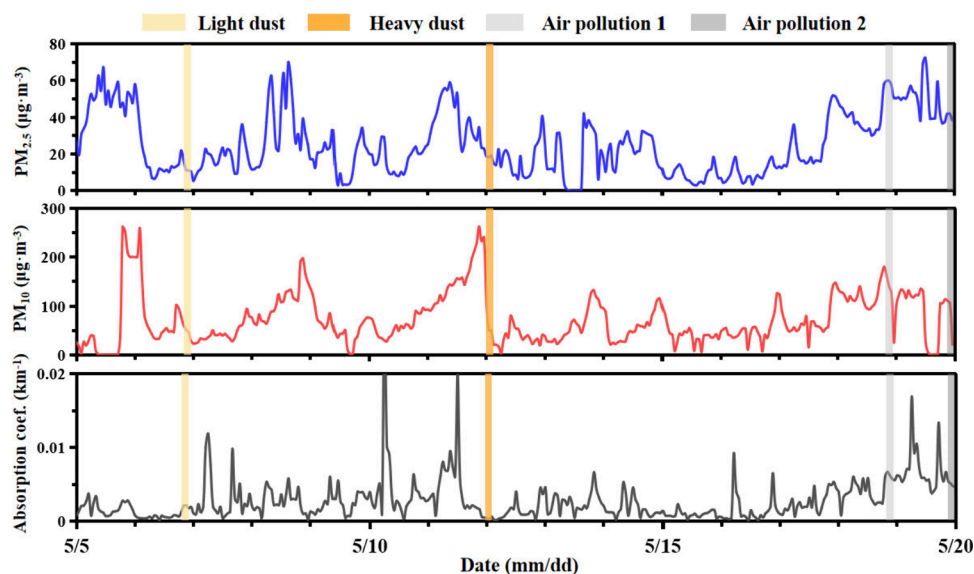


Figure 2. Variations of $PM_{2.5}$, PM_{10} , and absorption coefficients near the ground surface in May 2016 at Zhangbei ($114.7^{\circ}E$, $41.2^{\circ}N$) located in Northern China. The shadows indicate four typical cases that are further analyzed in Figures 3–4

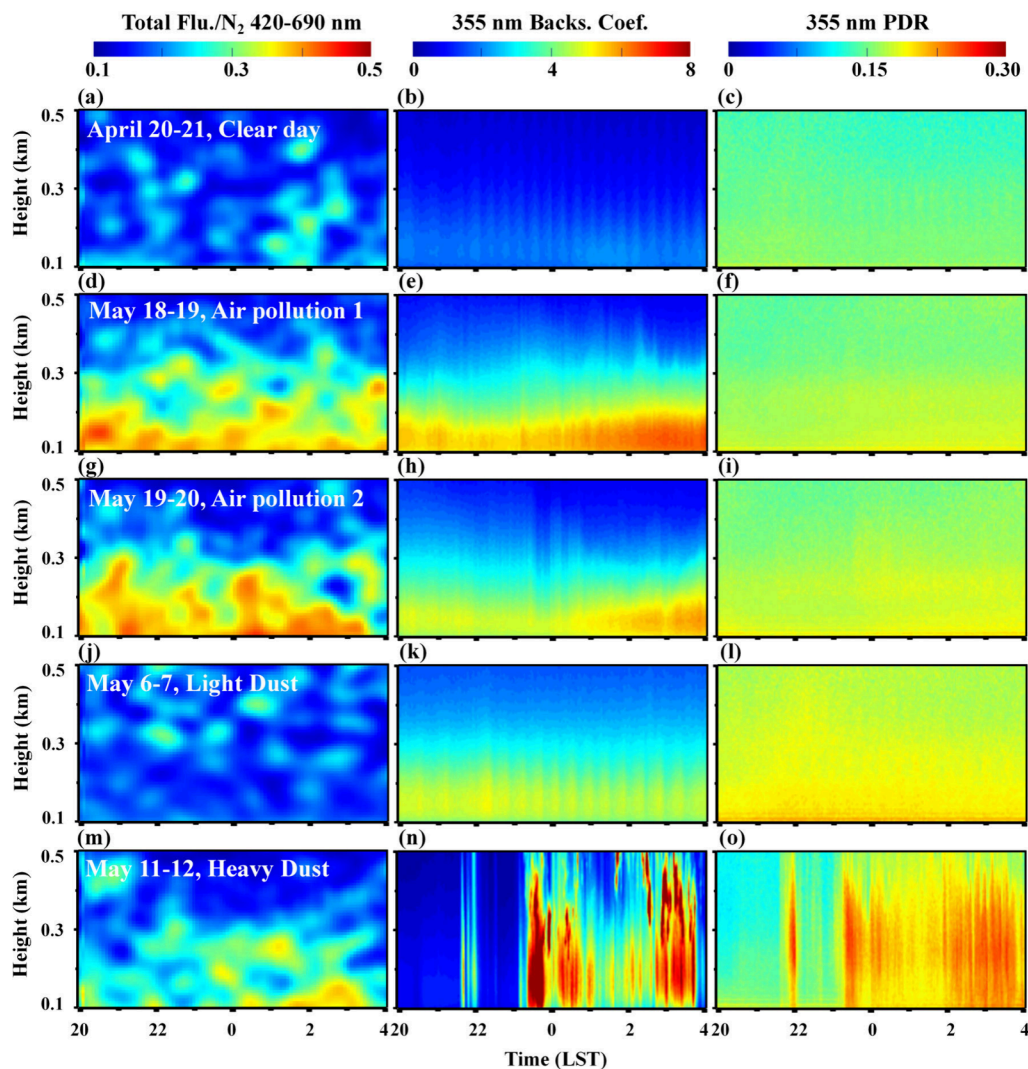


Figure 3. Vertical structure of the total fluorescence signal between 420 and 690 nm, backscattering coefficient, and particle depolarization ratio at 355 nm for five selected cases on April 20–21 (a–c), May 18–19 (d–f), May 19–20 (g–i), May 6–7 (j–l) and May 11–12 (m–o) 2016, respectively.

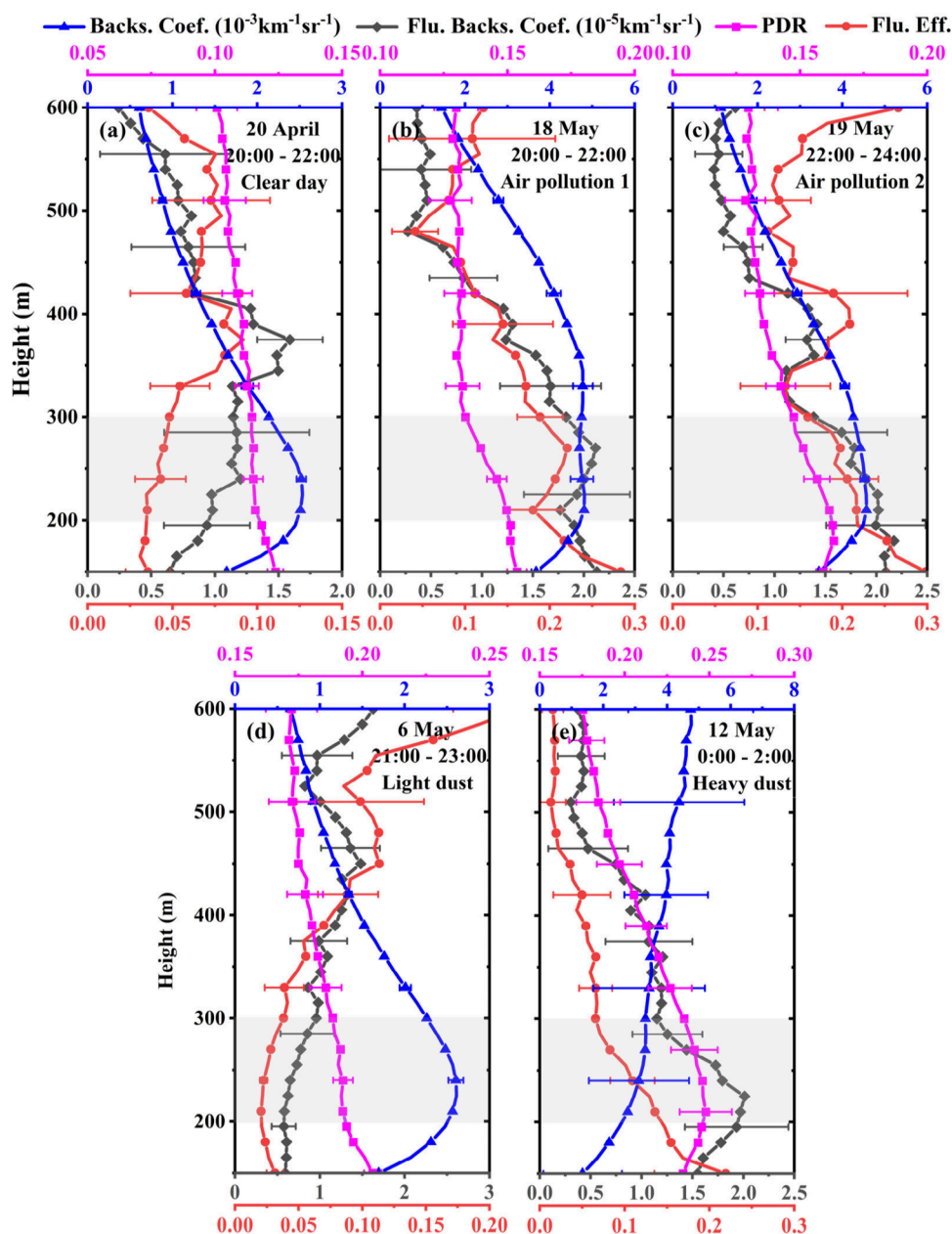


Figure 4. Averaged vertical profiles of the backscattering coefficient (blue), PDR (pink), fluorescence backscattering coefficient (black), and fluorescence efficiency (red) during five weather events: April 20–21(a), May 18–19 (b), May 19–20 (c), May 6–7 (d), and May 11–12 (e) 2016. Gray shadings are the selected aerosol layers for further analysis in Figure 5.

typical weather types based on lidar data and in situ measurements. Figure 2 displays in situ measurements from May 5 to 20, 2016. The orange shadows denote dust events, while the gray shadows indicate air pollution events. A clear day scenario was identified on April 20, with a $\text{PM}_{2.5}$ of $11 \mu\text{g}\cdot\text{m}^{-3}$, a PM_{10} of $42 \mu\text{g}\cdot\text{m}^{-3}$, and an absorption coefficient of $0.11 \times 10^{-2}\cdot\text{km}^{-1}$, coinciding with small values of the backscatter and particle depolarization ratio from lidar measurements.

3.1. Clear Day Case. During the night of April 20 (Figure 3a–c), the aerosol layer was confined below 300 m, exhibiting a weak lidar backscattering signal and a low PDR. Moreover, the broad fluorescence intensity, obtained by integrating the spectra from 420 to 690 nm, was relatively low, with a strength of less than 0.4. Notably, the 370–420 nm bands were omitted to minimize the impact of Raman scattering leakage

from the laser through long-pass filters. The averaged vertical profiles of aerosol parameters during the clear day, as observed on April 20, 2016, are depicted in Figure 4a. The backscattering coefficient from the lidar measurements did not exceed $2.4 \times 10^{-3} \text{ km}^{-1} \text{ sr}^{-1}$ within the detected range. Concurrently, the fluorescence backscattering coefficient within this layer was approximately $1.08 \times 10^{-5} \text{ km}^{-1} \text{ sr}^{-1}$.

3.2. Air Pollution Cases. Previous studies showed that the PDR of air pollution at 355 nm was 0.09 ± 0.04 in South Africa and 0.05 in Warsaw.^{45,46} In this study, air pollution cases were identified based on lidar and in situ measurements, showing high fluorescence intensity and high $\text{PM}_{2.5}$ but low PDR values. The temporal evolution of the normalized fluorescence intensity, backscattering coefficient, and PDR at 355 nm during nighttime air pollution on May 18–19, 2016, is depicted in Figure 3d–i. The height of the air pollutant layer

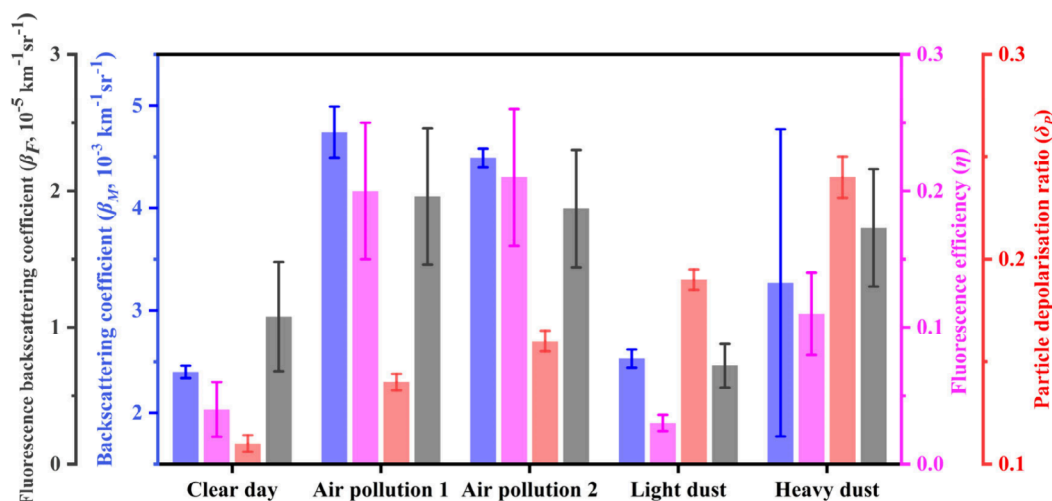


Figure 5. Comparison of the optical properties of fluorescent aerosol observed by the RPFSL under different weather conditions in Northern China during April and May of 2016.

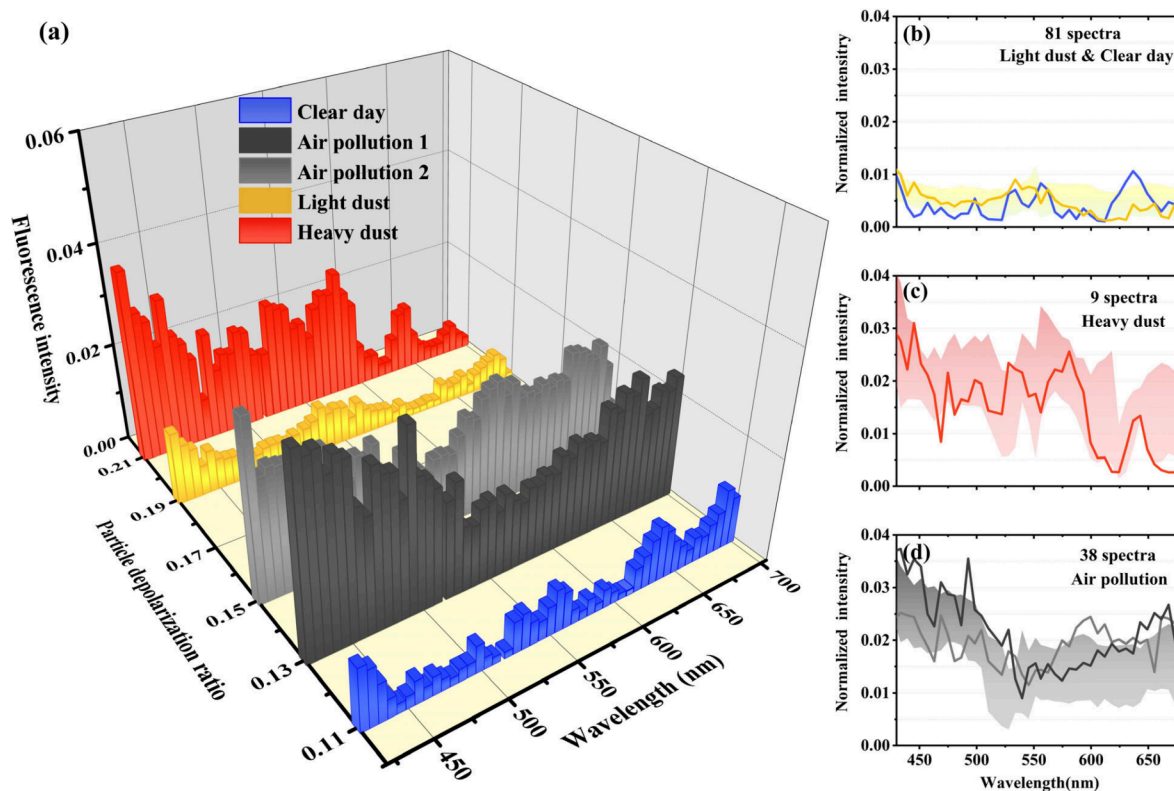


Figure 6. (a) The relation between the particle depolarization ratio (PDR) and fluorescence spectrum of atmospheric aerosols observed by the RPFSL under different weather conditions; (b-d) the mean and standard deviations of the normalized fluorescence spectra of atmospheric aerosols (shadows) measured in April - May 2016, and the template spectra in Figure 6a (solid lines, yellow is light dust, red is heavy dust, gray is air pollution, blue is clear day).

was below ~ 300 m, marked by a low PDR, a high backscattering coefficient, and a high fluorescence intensity. Figure 4b-c presents the vertical profiles of particle parameters for the two air pollution events. As the height increased, the pollution concentration decreased, the backscattering coefficient reduced from 5×10^{-3} to $2 \times 10^{-3} \text{ km}^{-1} \text{ sr}^{-1}$, and the PDR decreased from 0.15 to 0.12 in the 200–500 m range. Moreover, the fluorescence efficiency at the center of the aerosol layer was close to 0.2, respectively, which is significantly higher than the fluorescence efficiency observed

during the clear day. The fluorescence efficiency and fluorescence backscattering coefficient profiles were reasonably similar.

3.3. Dust Event Cases. We selected two dust events, on May 5–6 and May 11–12, to assess the variation in the fluorescence intensity of dust aerosols. Figure 3j-o illustrates the temporal evolution of the total fluorescence signal between 420 and 690 nm, the backscattering coefficient at 355 nm, and the particle depolarization ratio at 355 nm, as well as the

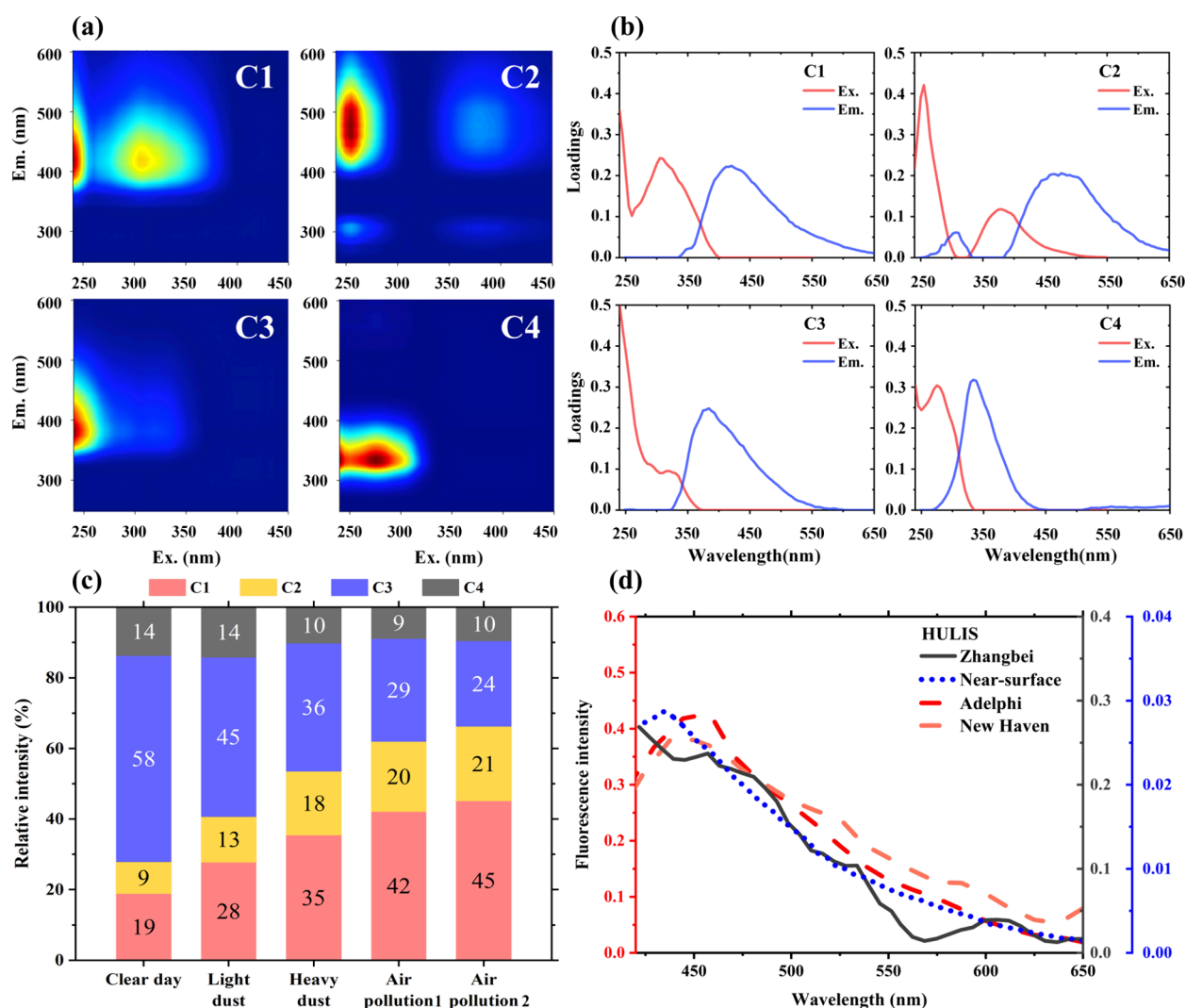


Figure 7. Four fluorescent components of ground-based aerosol samples under different weather conditions analyzed by EEM-PARAFAC (C1: low-oxygen HULIS; C2: high-oxygen HULIS; C3: phenols/tryptophan; C4: tyrosine), (a) the EEMs corresponding to each component, (b) the corresponding excitation and emission spectral loadings; (c) the relative abundance of each fluorescent component. (d) HULIS fluorescence spectra obtained from the PARAFAC decomposition of air pollution cases observed by the RPFSL (gray). Comparison with the HULIS fluorescence spectra decomposed from ground sampling (C1, blue) and HULIS spectra reported by Pan et al.⁶⁵ in Adelphi, MD and New Haven, CT (red).

corresponding vertical profiles of the main particle parameters, as shown in Figure 4d-e.

On May 6–7, a dust layer was identified at 100–300 m, with a low fluorescence signal. The backscattering coefficient was $2.18 \times 10^{-3} \text{ km}^{-1} \text{ sr}^{-1}$, and the PDR exceeded 0.19, indicating a light dust event. The heavy dust event occurring from May 11–12, 2016, was detected by the RPFSL, showing a large backscattering coefficient and a depolarization ratio at 355 nm, and suggesting that the dust event predominantly comprised highly nonspherical particles.^{47–49} A distinct dust layer was observed at 100–400 m; however, the corresponding depolarization ratio was lower than that of pure dust,²⁹ plausibly due to the mixing of transported dust particles with local aerosols. Additionally, a pronounced fluorescence signal was observed from 100 to 400 m between 23:00 and 03:00, with a fluorescence backscattering coefficient of $2 \times 10^{-5} \text{ km}^{-1} \text{ sr}^{-1}$. The backscattering coefficient increased from $\sim 2 \times 10^{-3}$ to $4 \times 10^{-3} \text{ km}^{-1} \text{ sr}^{-1}$. However, the fluorescence efficiency decreased with the altitude, from 0.2 (100 m) to 0.05 (400 m).

As shown in Figure 4d-e, it is clearly seen that dust weather contains a large number of fluorescent aerosols.⁵⁰

4. DISCUSSION

To further analyze the observed differences in retrieved lidar measurements under different weather conditions, we summarize the optical properties of fluorescent aerosol observed by the RPFSL during the investigation period as shown in Figure 5. We selected aerosol layers between 200 and 300 m above the ground during typical five weather conditions, then averaged four key optical parameters for 2 h of lidar measurements. It is shown that large scattering in optical properties occurs in different cases. For example, the values of fluorescence efficiency (η), PDR (δ_p), fluorescence backscattering coefficient (β_F), and backscattering coefficient (β_M) during heavy dust events were all large. The findings enabled us to categorize the following four types of particles: (I) clear day - low δ_p , low η , low β_M and low β_F ; (II) air pollution - middle δ_p , high η , high β_M and high β_F ; (III) light dust - high

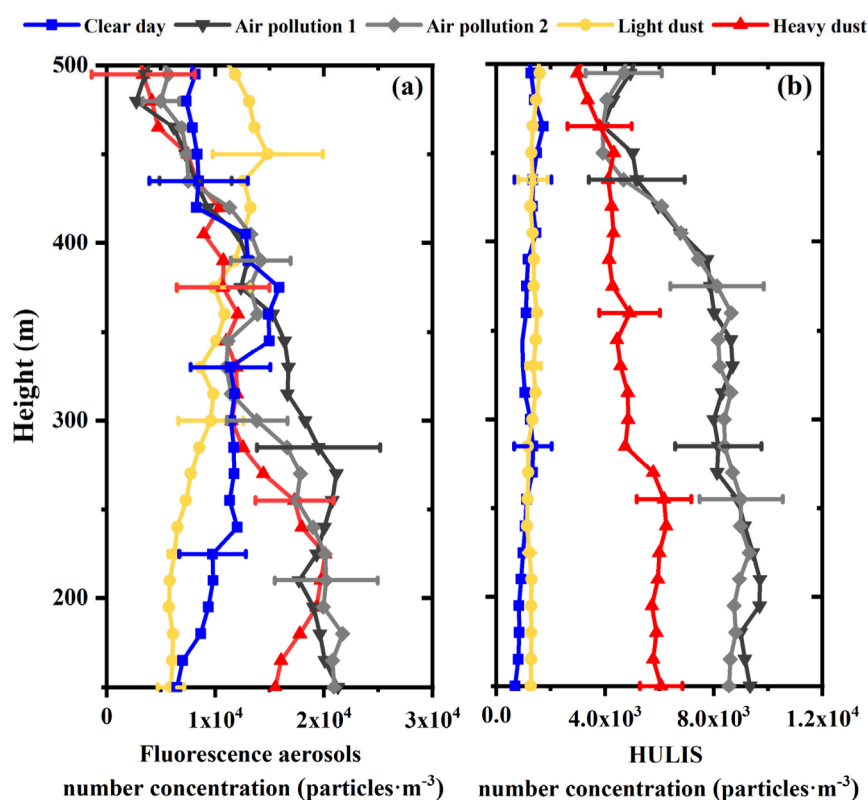


Figure 8. Vertical profiles of (a) total fluorescent aerosols and (b) HULIS concentration retrieved from the RPFSL measurements during five cases in the period April–May 2016.

δ_P , low η , low β_M , and low β_F ; and (IV) heavy dust - high δ_P , middle η , middle β_M , and high β_F .

The full-band fluorescence spectra of atmospheric aerosols ranging from 420 to 700 nm under five different weather conditions, as detected by the RPFSL, are shown in Figure 6a, indicating significant differences in the fluorescence intensity. Air pollution resulted in strong fluorescence across the entire spectral band, while the fluorescence intensity during clear day and light dust events was comparatively weak. The fluorescence spectrum of air pollutants exhibited a unimodal structure, with a peak appearing at 420 nm. The spectra of dust aerosols showed three obvious peaks around 420–440 nm, 550–570 nm, and 630–650 nm. The peak intensity was consistent with the dust concentration, i.e., the higher the dust concentration, the more intense the fluorescence peak. Moreover, the results demonstrated that different aerosol types, such as dust, air pollutants, and background aerosol, could be distinguished by combining PDR and fluorescence spectrum analyses. To verify the universal character of the selected weather cases, we used Hierarchical Cluster Analysis (HCA) to further classify all fluorescence spectra into four clusters.^{51,52} Figure 6b–d illustrates the results of matching the spectra recorded in April–May 2016 with templates shown in Figure 6a. Of the 240 total spectral profiles measured from April 20 to May 20, a total of 135 spectra were similar to at least one template spectrum in Figure 6a.

To validate the measurement of RPFSL, we analyzed the aerosol sampling data near the ground during the same period as the lidar observations. The method used in this study similar to that of Wen et al.,⁵³ EEM-PARAFAC is utilized to decompose four fluorescent components (Components 1–4, i.e., C1–C4), which include two HULIS fluorescent

components (C1 and C2) and two protein-like organic matter (PLOM) fluorescent components (C3 and C4). The EEM fluorescence fingerprint spectra of the four components obtained through PARAFAC decomposition are shown in Figure 7a–b. Then we can calculate the relative contributions of the C1–C4 components under different weather conditions, with the results as shown in Figure 7c. C1 (Ex./Em. = < 240(305)/420 nm) generally belongs to less oxygenated HULIS and is often reported in urban aerosols,⁵⁴ being associated with anthropogenic or terrestrial sources. In contrast, the fluorescence peak of C2 (Ex./Em. = 255(380)/476 nm) appears at a longer wavelength and is assigned to highly oxygenated HULIS, most likely originating from terrestrial and dust sources.^{55,56} The fluorescence of C3 (Ex./Em. = < 240(320)/383 nm) is typically associated with PLOM having a simple aromatic ring structure. However, recent studies have reported that phenolic compounds emit a fluorescence signal similar to that of C3, originating from the incomplete pyrolysis products of lignin and cellulose during biomass burning.^{57,58} C4 (Ex./Em. = < 240(275)/333 nm) closely resembles typical characteristics of tyrosine and may be a product of microbial activity in soil and dust.⁵⁹ Overall, C1 and C3 dominate the total fluorescence at Zhangbei, with a combined contribution exceeding 70%. The relative fluorescence contributions of HULIS represented by C1 and C2 substantially increased during dust and air pollution events. C3 was a significant contributor to the fluorophores, not only in dust events (40.5%) but also on clear day (58%). The relative intensity of C3 was slightly reduced during air pollution periods. In the five investigated cases, the contribution of C4 remained relatively unchanged, essentially around 10%. Remarkably, the five cases exhibited high fluorescence intensity

at 420–480 nm, Figure 6a, because the observation site was surrounded by rural areas, and the observation records showed that smoke from residential biomass burning, heating on fossil fuels, and cooking was common, suggesting that combustion produced a large amount of C1–C3.^{60,61} In the two dust cases, two shoulder peaks observed near 550–570 nm and 630–650 nm are significant: the fluorescence peak at 550–570 nm likely originates from an increase in the C3 content during dust events, which is related to phenolic compounds produced by biomass and coal combustion.⁶² The fluorescence peak at 630–650 nm is associated with luminescent compounds inherent in mineral dust and chlorophyll molecules present in various aerobic organisms in nature.^{63,64}

Components of C1 and C2, representing HULIS in air pollution cases, were significantly increased. It is noted that these two components account for more than 60% in fluorescence aerosols, as shown in Figure 7c. However, during dust events, none of the four analyzed components (C1–C4) had a dominant position. On clear day, the C3 contributes ~58% in fluorescence aerosols even though the total fluorescence intensity was weak. Therefore, high concentration of HULIS is clearly found during air pollution events. Furthermore, we applied PARAFAC for the spectral decomposition of 38 air pollution spectra, as shown in Figure 6d. Then, the obtained HULIS spectrum (gray line) was compared with the EEM results of ground-based samples and the previous study reported by Pan et al., as shown in Figure 7d. It is pointed out that Pan et al. used a dual-wavelength excitation particle fluorescence spectrometer to measure the fluorescence spectra from single atmospheric aerosol particles at New Haven, CT, and Adelphi, MD.⁶⁵ The fluorescence spectra of HULIS (dashed red line) were obtained after weighted averaging. We can clearly see that the variations of fluorescence spectra for these three independent samples are coincident, even though their detecting methods are largely different. Therefore, we conclude that HULIS can be reliably detected from the RPFSL observations in high altitude atmosphere according to the analysis of spectral results.

According to eq 5, the atmospheric total fluorescent aerosol concentration under different weather conditions can be retrieved from the total fluorescence signal (420–690 nm), as shown in Figure 8a. These concentration profiles represent the mean over a 2-h period. On clear day and light dust events, the concentrations of near-ground fluorescent aerosols were relatively low, with the peak concentration occurring above 350 m, amounting to 15891 particles·m⁻³ on the clear day and 14819 particles·m⁻³ on light dust events. In contrast, heavy dust and air pollution events exhibited significantly higher concentrations of fluorescent aerosols, which notably decreased with the altitude, from 20000 particles·m⁻³ at 200 m to 7000 particles·m⁻³ at 450 m. The vertical concentration profiles for HULIS were preliminarily assessed according to eq 8, as shown in Figure 8b. The HULIS concentrations during air pollution events were noticeably higher compared to other weather conditions, with the highest levels occurring at an altitude of 200 m. On May 18, the concentration peaked at 9699 particles·m⁻³, and on May 19, it was 9315 particles·m⁻³. As the altitude increases, the aerosols spread out, gradually decreasing the HULIS concentration. For heavy dust events, the HULIS concentration peaked at 240 m, being 6245 particles·m⁻³. In contrast, on clear day and light dust events, the HULIS concentration showed minimal variation with the

altitude, fluctuating within a narrow band of 1100 to 1300 particles·m⁻³.

■ ASSOCIATED CONTENT

Data Availability Statement

The data that have been used are confidential.

■ AUTHOR INFORMATION

Corresponding Author

Jiangping Huang – Key Laboratory for Semi-Arid Climate Change of the Ministry of Education, College of Atmospheric Sciences, Lanzhou University, Lanzhou 730000, China; Collaborative Innovation Center for West Ecological Safety (CIWES), Lanzhou University, Lanzhou 730000, China; orcid.org/0000-0003-2845-797X; Phone: +86 0931-8912979; Email: hjp@lzu.edu.cn

Authors

Zhongwei Huang – Key Laboratory for Semi-Arid Climate Change of the Ministry of Education, College of Atmospheric Sciences, Lanzhou University, Lanzhou 730000, China; Collaborative Innovation Center for West Ecological Safety (CIWES), Lanzhou University, Lanzhou 730000, China

Yongkai Wang – Key Laboratory for Semi-Arid Climate Change of the Ministry of Education, College of Atmospheric Sciences, Lanzhou University, Lanzhou 730000, China

Tian Zhou – Key Laboratory for Semi-Arid Climate Change of the Ministry of Education, College of Atmospheric Sciences, Lanzhou University, Lanzhou 730000, China

Yuanzong Ji – Key Laboratory for Semi-Arid Climate Change of the Ministry of Education, College of Atmospheric Sciences, Lanzhou University, Lanzhou 730000, China

Jianrong Bi – Key Laboratory for Semi-Arid Climate Change of the Ministry of Education, College of Atmospheric Sciences, Lanzhou University, Lanzhou 730000, China; Collaborative Innovation Center for West Ecological Safety (CIWES), Lanzhou University, Lanzhou 730000, China

Jinsen Shi – Key Laboratory for Semi-Arid Climate Change of the Ministry of Education, College of Atmospheric Sciences, Lanzhou University, Lanzhou 730000, China; Collaborative Innovation Center for West Ecological Safety (CIWES), Lanzhou University, Lanzhou 730000, China

Hui Wen – Key Laboratory for Semi-Arid Climate Change of the Ministry of Education, College of Atmospheric Sciences, Lanzhou University, Lanzhou 730000, China

Complete contact information is available at:

<https://pubs.acs.org/10.1021/acs.est.5c00028>

Notes

The authors declare no competing financial interest.

■ ACKNOWLEDGMENTS

This work was jointly supported by the National Natural Science Foundation of China (42427803, W2411029), the Gansu Science and Technology Major Program (24ZDWA006), and the Self-supporting Program of Guangzhou Laboratory (GZNL2024A01004). The authors thank the anonymous reviewers for improving the paper.

■ REFERENCES

(1) Voisin, D.; Jaffrezo, J. L.; Houdier, S.; Barret, M.; Cozic, J.; King, M. D.; France, J. L.; Reay, H. J.; Grannas, A.; Kos, G.; et al. Carbonaceous species and humic like substances (HULIS) in Arctic

- snowpack during OASIS field campaign in Barrow. *J. Geophys. Res. Atmos.* **2012**, *117*, D14.
- (2) Feczko, T.; Puxbaum, H.; Kasper-Giebl, A.; Handler, M.; Limbeck, A.; Gelencser, A.; Pio, C.; Preunkert, S.; Legrand, M. Determination of water and alkaline extractable atmospheric humic-like substances with the TU Vienna HULIS analyzer in samples from six background sites in Europe. *J. Geophys. Res. Atmos.* **2007**, *112*, D23.
- (3) Duarte, R.; Santos, E.; Pio, C. A.; Duarte, A. C. Comparison of structural features of water-soluble organic matter from atmospheric aerosols with those of aquatic humic substances. *Atmos. Environ.* **2007**, *41*, 8100–8113.
- (4) Win, M. S.; Tian, Z.; Zhao, H.; Xiao, K.; Peng, J.; Shang, Y.; Wu, M.; Xiu, G.; Lu, S.; Yonemochi, S.; Wang, Q. Atmospheric HULIS and its ability to mediate the reactive oxygen species (ROS): A review. *Journal of Environmental Sciences. J. Environ. Sci.* **2018**, *71*, 13–31.
- (5) Ma, Y.; Cheng, Y.; Qiu, X.; Cao, G.; Fang, Y.; Wang, J.; Zhu, T.; Yu, J.; Hu, D. Sources and oxidative potential of water-soluble humic-like substances (HULIS WS) in fine particulate matter (PM 2.5) in Beijing. *Atmos. Chem. Phys.* **2018**, *18* (8), 5607–5617.
- (6) El Haddad, I.; Marchand, N.; Dron, J.; Temime-Roussel, B.; Quivet, E.; Wortham, H.; Jaffrezo, J. L.; Baduel, C.; Voisin, D.; Besombes, J. L.; et al. Comprehensive primary particulate organic characterization of vehicular exhaust emissions in France. *Atmos. Chem. Phys.* **2009**, *43* (39), 6190–6198.
- (7) Cavalli, F.; Facchini, M.; Decesari, S.; Mircea, M.; Emblico, L.; Fuzzi, S.; Ceburnis, D.; Yoon, Y.; O'Dowd, C.; Putaud, J. P.; et al. Advances in characterization of size-resolved organic matter in marine aerosol over the North Atlantic. *J. Geophys. Res. Atmos.* **2004**, *109*, D24.
- (8) Salma, I.; Mészáros, T.; Maenhaut, W. Mass size distribution of carbon in atmospheric humic-like substances and water soluble organic carbon for an urban environment. *J. Aerosol Sci.* **2013**, *56*, 53–60.
- (9) Dinar, E.; Taraniuk, I.; Graber, E.; Katsman, S.; Moise, T.; Anttila, T.; Mentel, T.; Rudich, Y. Cloud Condensation Nuclei properties of model and atmospheric HULIS. *Atmos. Chem. Phys.* **2006**, *6*, 2465–2482.
- (10) Dou, J.; Lin, P.; Kuang, B. Y.; Yu, J. Z. Reactive oxygen species production mediated by humic-like substances in atmospheric aerosols: enhancement effects by pyridine, imidazole, and their derivatives. *Environ. Sci. Technol.* **2015**, *49*, 6457–6465.
- (11) Wang, B.; Knopf, D. A. Heterogeneous ice nucleation on particles composed of humic-like substances impacted by O₃. *J. Geophys. Res. Atmos.* **2011**, *116*, D3.
- (12) Hoffer, A.; Gelencsér, A.; Guyon, P.; Kiss, G.; Schmid, O.; Frank, G.; Artaxo, P.; Andreae, M. Optical properties of humic-like substances (HULIS) in biomass-burning aerosols. *Atmos. Chem. Phys.* **2006**, *6* (11), 3563–3570.
- (13) Varga, B.; Kiss, G.; Ganszky, I.; Gelencser, A.; Krivacsy, Z. Isolation of water-soluble organic matter from atmospheric aerosol. *Talanta* **2001**, *55*, 561.
- (14) Góra, R.; Hutta, M. Reversed-phase liquid chromatographic characterization and analysis of air particulates humic (-like) substances in presence of pollens. *J. Chromatogr. A* **2005**, *1084*, 39–45.
- (15) Krivácsy, Z.; Kiss, G.; Varga, B.; Galambos, I.; Sárvári, Z.; Gelencsér, A.; Molnár, A.; Fuzzi, S.; Facchini, M. C.; Zappoli, S.; Andracchio, A.; Alsberg, T.; Hansson, H. C.; Persson, L. Study of humic-like substances in fog and interstitial aerosol by size-exclusion chromatography and capillary electrophoresis. *Atmos. Environ.* **2000**, *34*, 4273–4281.
- (16) Stone, E. A.; Hedman, C. J.; Sheesley, R. J.; Shafer, M. M.; Schauer, J. J. Investigating the chemical nature of humic-like substances (HULIS) in North American atmospheric aerosols by liquid chromatography tandem mass spectrometry. *Atmos. Environ.* **2009**, *43* (27), 4205–4213.
- (17) Andracchio, A.; Cavicchi, C.; Tonelli, D.; Zappoli, S. A new approach for the fractionation of water-soluble organic carbon in atmospheric aerosols and cloud drops. *Atmos. Environ.* **2002**, *36*, 5097–5107.
- (18) Graber, E. R.; Rudich, Y. Atmospheric HULIS: How humic-like are they? A comprehensive and critical review. *Atmos. Chem. Phys.* **2006**, *6*, 729–753.
- (19) Chen, Q.; Miyazaki, Y.; Kawamura, K.; Matsumoto, K.; Coburn, S.; Volkamer, R.; Iwamoto, Y.; Kagami, S.; Deng, Y.; Ogawa, S.; Ramasamy, S.; Kato, S.; Ida, A.; Kajii, Y.; Mochida, M. Characterization of Chromophoric Water-Soluble Organic Matter in Urban, Forest, and Marine Aerosols by HR-ToF-AMS Analysis and Excitation-Emission Matrix Spectroscopy. *Environ. Sci. Technol.* **2016**, *50*, 10351–10360.
- (20) Yue, S.; Li, L.; Xu, W.; Zhao, J.; Ren, H.; Ji, D.; Li, P.; Zhang, Q.; Wei, L.; Xie, Q.; Pan, X.; Wang, Z.; Sun, Y.; Fu, P. Biological and Nonbiological Sources of Fluorescent Aerosol Particles in the Urban Atmosphere. *Environ. Sci. Technol.* **2022**, *56*, 7588–7597.
- (21) Chen, Q.; Hua, X.; Wang, Y.; Zhang, L.; Chang, T. Semi-continuous measurement of chromophoric organic aerosols using the PILS-EEM-TOC system. *Atmos. Environ.* **2021**, *244*, 117941.
- (22) Zhao, M. F.; Qiao, T.; Li, Y. L.; Tang, X. X.; Xiu, G. L.; Yu, J. Z. Temporal variations and source apportionment of HULIS-C in PM_{2.5} in urban Shanghai. *Sci. Total Environ.* **2016**, *571*, 18–26.
- (23) Huang, Z.; Wang, Y.; Bi, J.; Wang, T.; Li, W.; Li, Z.; Zhou, T. An overview of aerosol lidar: Progress and prospect. *National Remote Sensing Bulletin* **2022**, *26*, 834.
- (24) Wang, Y.; Huang, Z.; Zhou, T.; Bi, J.; Shi, J. Identification of fluorescent aerosol observed by a spectroscopic lidar over northwest China. *Opt. Express* **2023**, *31*, 22157–22169.
- (25) Saito, Y.; Ichihara, K.; Morishita, K.; Uchiyama, K.; Kobayashi, F.; Tomida, T. Remote detection of the fluorescence spectrum of natural pollens floating in the atmosphere using a laser-induced-fluorescence spectrum (lifs) lidar. *Remote Sens.* **2018**, *10*, 1533.
- (26) Qi, J.; Huang, Z.; Maki, T.; Kang, S.; Guo, J.; Liu, K.; Liu, Y. Airborne bacterial communities over the Tibetan and Mongolian Plateaus: variations and their possible sources. *Atmospheric Research* **2021**, *247*, 105215.
- (27) Tang, K.; Huang, Z.; Huang, J.; Maki, T.; Zhang, S.; Shimizu, A.; et al. Characterization of atmospheric bioaerosols along the transport pathway of Asian dust during the Dust-Bioaerosol 2016 Campaign. *Atmos. Chem. Phys.* **2018**, *18*, 7131–7148.
- (28) Huang, Z.; Yu, X.; Liu, Q.; Maki, T.; Alam, K.; Wang, Y.; Xue, F.; Tang, S.; Du, P.; Dong, Q.; Wang, D.; Huang, J. Bioaerosols in the atmosphere: A comprehensive review on detection methods, concentration and influencing factors. *Sci. Total Environ.* **2024**, *912*, 168818.
- (29) Freudenthaler, V.; Esselborn, M.; Wiegner, M.; Heese, B.; Seefeldne, M.; et al. Depolarization ratio profiling at several wavelengths in pure Saharan dust during SAMUM 2006. *Tellus B* **2009**, *61*, 165–179.
- (30) Zhang, S.; Huang, Z.; Alam, K.; Li, M.; Dong, Q.; Wang, Y.; Shen, X.; Bi, J.; Zhang, J.; Li, W.; Li, Z.; Wang, W.; Cui, Z.; Song, X. Derived Profiles of CCN and INP Number Concentrations in the Taklimakan Desert via Combined Polarization Lidar, Sun-Photometer, and Radiosonde Observations. *Remote Sens.* **2023**, *15*, 1216.
- (31) Ansmann, A.; Riebesell, M.; Wandinger, U.; Weitkamp, C.; Voss, E. Combined raman elastic-backscatter LIDAR for vertical profiling of moisture, aerosol extinction, backscatter, and LIDAR ratio. *Appl. Phys. B: Laser Opt.* **1992**, *55*, 18–28.
- (32) Veselovskii, I.; Hu, Q.; Goloub, P.; Podvin, T.; Korenskiy, M.; Pujol, O.; Dubovik, O.; Lopatin, A. Combined use of Mie–Raman and fluorescence lidar observations for improving aerosol characterization: feasibility experiment. *Atmos. Meas. Technol.* **2020**, *13*, 6691–6701.
- (33) Qi, S.; Huang, Z.; Ma, X.; Huang, J.; Zhou, T.; Zhang, S.; Dong, Q.; Bi, J.; Shi, J. Classification of atmospheric aerosols and clouds by use of dual-polarization lidar measurements. *Opt. Express* **2021**, *29*, 23461–23476.
- (34) Dong, Q.; Huang, Z.; Li, W.; Li, Z.; Song, X.; Liu, W.; Wang, T.; Bi, J.; Shi, J. Polarization Lidar Measurements of Dust Optical

Properties at the Junction of the Taklimakan Desert-Tibetan Plateau. *Remote Sens.* **2022**, *14*, 558.

(35) Zhang, S.; Huang, Z.; Li, M.; Shen, X.; Wang, Y.; Dong, Q.; Bi, J.; Zhang, J.; Li, W.; Li, Z.; Song, X. Vertical Structure of Dust Aerosols Observed by a Ground-Based Raman Lidar with Polarization Capabilities in the Center of the Taklimakan Desert. *Remote Sens.* **2022**, *14*, 2461.

(36) Huang, Z.; Dong, Q.; Chen, B.; Wang, T.; Bi, J.; Zhou, T.; Alam, K.; Shi, J.; Zhang, S. Method for retrieving range-resolved aerosol microphysical properties from polarization lidar measurements. *Opt. Express* **2023**, *31*, 7599–7616.

(37) Liu, Z.; Sugimoto, N.; Murayama, T. Extinction-to-backscatter ratio of Asian dust observed with high-spectral-resolution lidar and Raman lidar. *Appl. Opt.* **2002**, *41*, 2760–2767.

(38) Behrendt, A.; Nakamura, T. Calculation of the calibration constant of polarization lidar and its dependency on atmospheric temperature. *Opt. Express* **2002**, *10*, 805–817.

(39) Sugimoto, N.; Huang, Z.; Nishizawa, T.; Matsui, I.; Tatarov, B. Fluorescence from atmospheric aerosols observed with a multi-channel lidar spectrometer. *Opt. Express* **2012**, *20*, 20800–20807.

(40) Dubovik, O.; Holben, B. N.; Eck, T. F.; Smirnov, A.; Slutsker, I.; et al. Variability of Absorption and Optical Properties of Key Aerosol Types Observed in Worldwide Locations. *J. Atmos. Sci.* **2002**, *59*, 590–608.

(41) Kristensen, T. B.; Du, L.; Nguyen, Q. T.; Nøjgaard, J. K.; Koch, C. B.; Nielsen, O. F.; Hallar, A.; Lowenthal, D.; Nekat, B.; Pinxteren, D.; et al. Chemical properties of HULIS from three different environments. *Atmos. Chem. Phys.* **2015**, *72*, 65–80.

(42) Pan, Y. L.; Hill, S. C.; Santarpia, J. L.; Brinkley, K.; Sickler, T.; Coleman, M.; Williamson, C.; Gurton, K.; Felton, M.; Pinnick, R. G.; Baker, N.; Eshbaugh, J.; Hahn, J.; Smith, E.; Alvarez, B.; Prugh, A.; Gardner, W. Spectrally-resolved fluorescence cross sections of aerosolized biological live agents and simulants using five excitation wavelengths in a BSL-3 laboratory. *Opt. Express* **2014**, *22* (7), 8165–89.

(43) Rao, Z.; He, T.; Hua, D.; Wang, Y.; Wang, X.; Chen, Y.; Le, J. Preliminary measurements of fluorescent aerosol number concentrations using a laser-induced fluorescence lidar. *Appl. Opt.* **2018**, *57* (25), 7211–7215.

(44) Murphy, K. R.; Stedmon, C. A.; Graeber, D.; Bro, R. Fluorescence spectroscopy and multi-way techniques. *PARAFAC. Analytical Methods* **2013**, *5*, 6557–6566.

(45) Giannakaki, E.; Zyl, P. G. V.; Müller, D.; Balis, D.; Komppula, M. Optical and microphysical characterization of aerosol layers over South Africa by means of multi-wavelength depolarization and Raman lidar measurements. *Atmos. Chem. Phys.* **2016**, *16*, 8109–8123.

(46) Janicka, L.; Stachlewska, I. S. Properties of biomass burning aerosol mixtures derived at fine temporal and spatial scales from Raman lidar measurements: Part I optical properties. *Atmos. Chem. Phys.* **2019**, *19*, 3877–3902.

(47) Huang, Z.; Nee, J.; Chiang, C.; Zhang, S.; Jin, H.; Wang, W.; Zhou, T. Real-Time Observations of Dust–Cloud Interactions Based on Polarization and Raman Lidar Measurements. *Remote Sens.* **2018**, *10*, 1017.

(48) Huang, Z.; Dong, Q.; Xue, F.; Qi, J.; Yu, X.; Maki, T.; Du, P.; Gu, Q.; Tang, S.; Shi, J.; Bi, J.; Zhou, T.; Huang, J. Large-scale Dust-Bioaerosol field observations in East Asia. *Bull. Am. Meteorol. Soc.* **2024**, *105* (3), No. E501.

(49) Huang, Z.; Qi, S.; Zhou, T.; Dong, Q.; Ma, X.; Zhang, S.; Bi, J.; Shi, J. Investigation of aerosol absorption with dual-polarization lidar observations. *Opt. Express* **2020**, *28*, 7028–7035.

(50) Sugimoto, N.; Huang, Z. Lidar Methods for Observing Mineral Dust. *J. Meteor. Res.* **2014**, *28* (2), 173–184.

(51) Pinnick, R. G.; Fernandez, E.; Rosen, J. M.; Hill, S. C.; Wang, Y.; Pan, Y. L. Fluorescence spectra and elastic scattering characteristics of atmospheric aerosol in Las Cruces, New Mexico, USA: Variability of concentrations and possible constituents and sources of particles in various spectral clusters. *Atmos. Environ.* **2013**, *65*, 195–204.

(52) Pan, Y.; Pinnick, R.; Hill, S.; Rosen, J.; Chang, R. Single-particle laser-induced-fluorescence spectra of biological and other organic-carbon aerosols in the atmosphere: Measurements at New Haven, Connecticut, and Las Cruces, New Mexico. *J. Geophys. Res.* **2007**, *112*, D07207.

(53) Wen, H.; Zhou, Y.; Xu, X.; Wang, T.; Chen, Q.; Chen, Q.; Li, W.; Wang, Z.; Huang, Z.; Zhou, T.; Shi, J.; Bi, J.; Ji, M.; Wang, X. Water-soluble brown carbon in atmospheric aerosols along the transport pathway of Asian dust: Optical properties, chemical compositions, and potential sources. *Sci. Total Environ.* **2021**, *789*, 147971.

(54) Wang, H.; Zhang, L.; Huo, T.; Wang, B.; Yang, F.; Chen, Y.; Tian, M.; Qiao, B.; Peng, C. Application of parallel factor analysis model to decompose excitation-emission matrix fluorescence spectra for characterizing sources of water-soluble brown carbon in PM_{2.5}. *Atmos. Environ.* **2020**, *223*, 117192.

(55) Chen, Q.; Ikemori, F.; Mochida, M. Light Absorption and Excitation-Emission Fluorescence of Urban Organic Aerosol Components and Their Relationship to Chemical Structure. *Environ. Sci. Technol.* **2016**, *50*, 10859–10868.

(56) Chen, Q.; Li, J.; Hua, X.; Jiang, X.; Mu, Z.; Wang, M.; Wang, J.; Shan, M.; Yang, X.; Fan, X.; Song, J.; Wang, Y.; Guan, D.; Du, L. Identification of species and sources of atmospheric chromophores by fluorescence excitation-emission matrix with parallel factor analysis. *Sci. Total Environ.* **2020**, *718*, 137322.

(57) Cory, R. M.; McKnight, D. M. Fluorescence spectroscopy reveals ubiquitous presence of oxidized and reduced quinones in dissolved organic matter. *Environ. Sci. Technol.* **2005**, *39*, 8142–8149.

(58) Fan, X.; Cao, T.; Yu, X.; Wang, Y.; Xiao, X.; Li, F.; Xie, Y.; Ji, W.; Song, J.; Peng, P. The Evolutionary Behavior of Chromophoric Brown Carbon During Ozone Aging of Fine Particles from Biomass Burning. *Atmos. Chem. Phys.* **2020**, *20* (8), 4593–4605.

(59) Zhou, Y.; Wen, H.; Liu, J.; Pu, W.; Chen, Q.; Wang, X. The optical characteristics and sources of chromophoric dissolved organic matter (CDOM) in seasonal snow of northwestern China. *Cryosphere* **2019**, *13*, 157–175.

(60) Tang, J.; Li, J.; Su, T.; Han, Y.; Mo, Y.; Jiang, H.; Cui, M.; Jiang, B.; Chen, Y.; Tang, J.; Song, J.; Peng, P.; Zhang, G. Molecular compositions and optical properties of dissolved brown carbon in biomass burning, coal combustion, and vehicle emission aerosols illuminated by excitation–emission matrix spectroscopy and Fourier transform ion cyclotron resonance mass spectrometry analysis. *Atmos. Chem. Phys.* **2020**, *20*, 2513–2532.

(61) Fan, X.; Wei, S.; Zhu, M.; Song, J.; Peng, P. Comprehensive characterization of humic-like substances in smoke PM_{2.5} emitted from the combustion of biomass materials and fossil fuels. *Atmos. Chem. Phys.* **2016**, *16* (20), 13321–13340.

(62) Roshchina, V.; Mel'nikova, E.; Kovaleva, L. Changes in fluorescence during development of the male gametophyte. *Russ. J. Plant Physiol.* **1997**, *44*, 36–44.

(63) O'Connor, D. J.; Lovera, P.; Iacopino, D.; O'Riordan, A.; Healy, D. A.; Sodeau, J. R. Using spectral analysis and fluorescence lifetimes to discriminate between grass and tree pollen for aerobiological applications. *Anal. Methods* **2014**, *6*, 1633–1639.

(64) Bozlee, B. J.; Misra, A. K.; Sharma, S. K.; Ingram, M. Remote Raman and fluorescence studies of mineral samples. *Spectrochim. Acta Part A* **2005**, *61*, 2342–2348.

(65) Pan, Y.; Huang, H.; Chang, R. K. Clustered and integrated fluorescence spectra from single atmospheric aerosol particles excited by a 263- and 351-nm laser at New Haven, CT, and Adelphi, MD. *J. Quant. Spectrosc. Radiat. Transfer* **2012**, *113*, 2213–2221.